ADVANCED ENERGY MATERIALS
www.advenergymat.de

Exceeding Single-Pass Equilibrium with Integrated Absorption Separation for Ammonia Synthesis Using Renewable Energy—Redefining the Haber-Bosch Loop

*Collin Smith and Laura Torrente-Murciano**

The synthesis of ammonia through the Haber-Bosch process has been at the foundation of the chemical industry for over 100 years, but when the energy and feedstock sources switch from fossil fuels to renewable electricity, the process needs to be reimagined. Herein, the successful integration of ammonia synthesis and separation is demonstrated in a recycle-less process setting the foundations of green ammonia technology. The ruthenium-based catalyst uses a nanostructured CeO_2 support and Cs electronic promotion to remove hydrogen and ammonia inhibition, respectively, creating a catalyst with low-temperature (<300 °C) activity that quickly approaches equilibrium. The absorbent uses $MnCl_2$ to avoid the acid releasing decomposition of conventional absorbents like $MgCl_2$, and a support of SiO_2 to simultaneously enhance $MnCl_2$ dispersion and improve stabilization. This integrated catalyst-absorbent system reproducibly exceeds single-pass ammonia synthesis equilibrium. Kinetic models of the catalyst and absorbent successfully predict the experimental long-term behavior and facilitate the design of an integrated system. These results present a framework for aligning intermittent and isolated renewable energy with ammonia synthesis by decreasing capital complexity and increasing process agility—adapting to a shifting energy landscape to continue providing fertilizers with minimum CO_2 penalty and pioneer energy storage.

1. Introduction

Ammonia has been a foundational chemical for human civilization since it was first synthesized industrially in the early 20th century. Its role as the primary component in synthetic fertilizers is responsible for the continued population growth in the last century.[1] The core Haber-Bosch (HB) process consists of the conversion of nitrogen and hydrogen at high temperature (>400 °C) and pressure (>100 bar) using an iron-based catalyst. These conditions favor a sensible kinetic rate at the expense of low conversions (<20%) due to the thermodynamic limitations. The reactor effluent is cooled, ammonia is condensed and the remainder is recycled in order to increase the hydrogen yield. While the core process looks very similar today as it did 100 years ago, the process equipment has been optimized for consuming fossil fuels (mainly methane) as the hydrogen feedstock and utilizing the high-grade steam generated as a by-product to power equipment leading to high CO_2 emissions (1.7 $t_{CO2}.t_{NH3}^{-1}$).[2] In recent decades, the availability of renewable electricity and the desire for a general electrification of the chemical industry has revealed that industrial ammonia synthesis is operating at a false optimization when only fossil fuels are considered as an energy source. If ammonia synthesis can be effectively coupled with renewable electricity, it will not only lead to sustainable fertilizer but it will also open avenues for ammonia as a dense energy storage and potentially a new energy market.[3]

The electric HB process, which produces hydrogen through electrolysis rather than from fossil fuels, can operate entirely from renewable energy with considerable lower CO_2 emissions (0.4 $t_{CO2}.t_{NH3}^{-1}$) partially thanks to the use of highly efficient electric compressors rather than steam turbines.[2] However, renewable energy can be frustratingly isolated and intermittent; therefore making it incompatible with the conventional HB process intended to operate at steady-state conditions for months using capital-intensive equipment. Currently, large battery stores and hydrogen tanks are required to create and interface between fluctuating renewable energy and a steady industrial process. A new small-scale and agile process is required to re-imagine the relationship between renewable energy and ammonia. In recent years, the focus of innovation has been on decreasing the operating pressure of ammonia synthesis to ≈20 bar as well as replacing the ammonia condensation separation by absorption.[4] Within this context, metal halides such as $MgCl_2$ and $CaCl_2$ can operate at high temperatures (>300 °C) relative to conventional adsorbents,[5,6] making potentially possible the combination of catalyst and absorbent in the same vessel for in situ ammonia separation—removing equilibrium limitations and the need to recycle unreacted nitrogen and

C. Smith, Dr. L. Torrente-Murciano
Department of Chemical Engineering and Biotechnology
University of Cambridge
Philippa Fawcett Drive, Cambridge CB3 0AS, UK
E-mail: lt416@cam.ac.uk

The ORCID identification number(s) for the author(s) of this article can be found under https://doi.org/10.1002/aenm.202003845.

DOI: 10.1002/aenm.202003845

hydrogen, as has been theoretically suggested previously.[7] This technology simplifies the capital requirements of the process and the ability to adjust steady-state.

Herein, we demonstrate for the first time the experimental feasibility of the integration of the synthesis and separation of ammonia by combining a catalyst and an absorbent to exceed single-pass equilibrium. A suitable ruthenium-based catalyst is designed using nanostructured ceria as support and cesium as electronic promoter capable of achieving low-temperature (<300 °C) ammonia synthesis, overcoming the conventional hydrogen inhibition of previously reported catalysts and quickly approaching equilibrium at moderate pressure (20 bar). A unique absorbent is synthesized from $MnCl_2$ supported on silica gel with enhanced stability and resistance to decomposition. Kinetic models developed for both reaction and absorption steps separately enable the optimization of the integrated process to maximize the overall hydrogen conversion >90% in the re-defined Haber-Bosch process.

2. Results and Discussion

2.1. Catalyst Development and Kinetic Model

The vision of an integrated ammonia synthesis and separation process requires the design of a catalyst active at low temperature and pressures while presenting a high rate of reaction. We have achieved this with ruthenium nanoparticles supported on nanostructured ceria rods and promoted by cesium. Ruthenium is well known to be the most active metal for ammonia synthesis at low pressures.[8] The active sites are believed to be formed by a specific combination of 5 atoms, called B_5, whose concentration is maximized on small nanoparticles (≈2–5 nm),[9–11] which makes supporting ruthenium on high surface area structures a necessity. **Figure 1**e shows the comparison of the catalytic activity at 20 barg of Ru nanoparticles supported on typical supports such as alumina (Al_2O_3) or carbon nanotubes (CNT) in comparison to nanostructured ceria. Both Al_2O_3 and CNT supported catalysts indicated low activity below 350 °C because ruthenium is normally severely

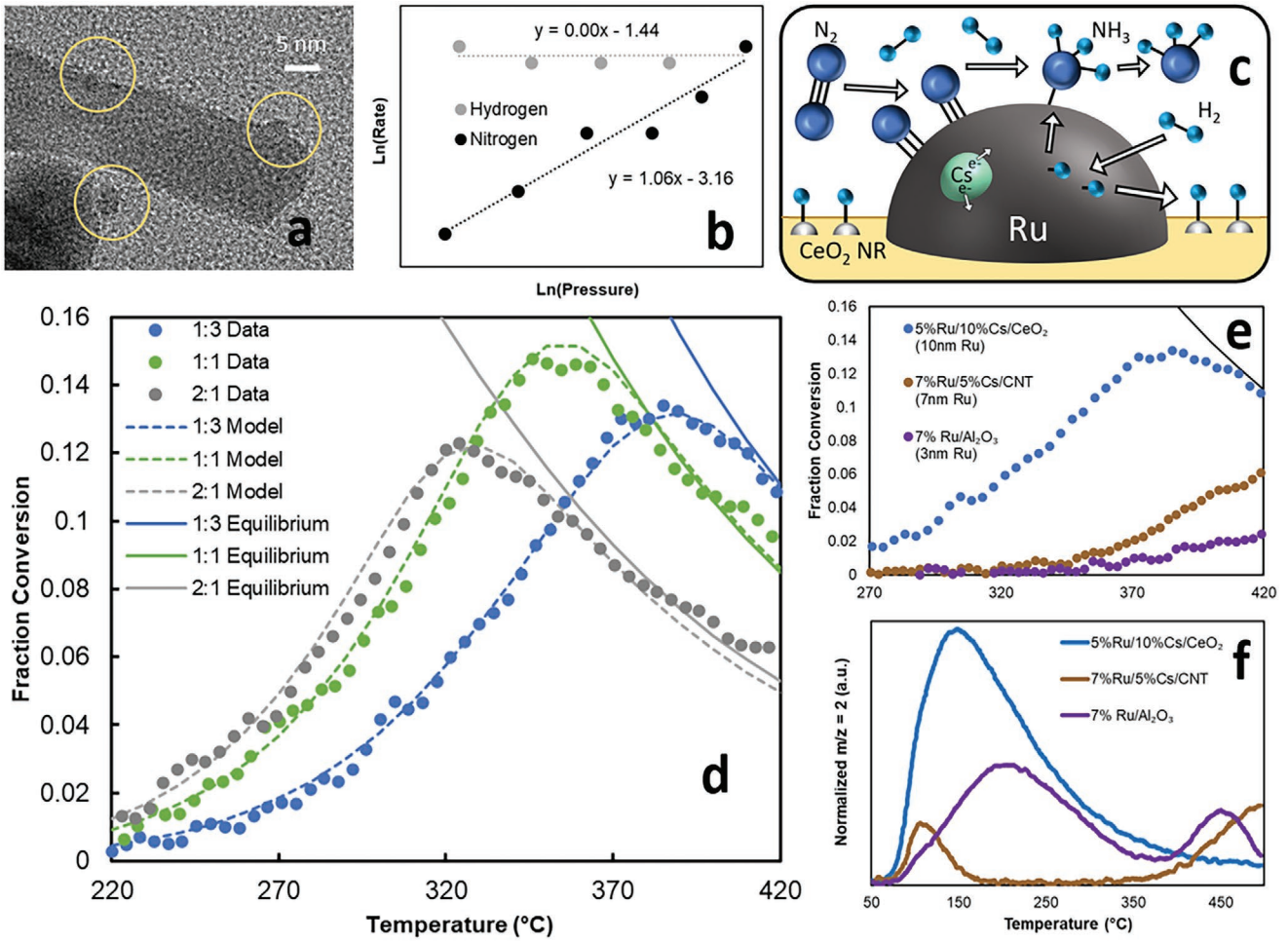

Figure 1. Reaction kinetics for 5%Ru/10%Cs/CeO_2 catalyst. a) TEM of 5%Ru/10%Cs/CeO_2 with well anchored Ru particles. b) Determination of reaction order for N_2 (1) and H_2 (0) where the slope of the linear fit is the reaction order. c) Schematic of ammonia synthesis over catalyst with ceria removing hydrogen from the surface and cesium adding electronic promotion. d) Fractional conversion of 5%Ru/10%Cs/CeO_2 at 20 barg (11.7 SCCM; GHSV 3.6 h^{-1}) as a function of temperature and N_2:H_2 ratio. Solid lines show thermodynamic equilibrium at different N_2:H_2 ratio. e) Comparison of fractional conversion for different Ru-based catalysts as a function of temperature at 20 barg where Ru particle size is determined using CO chemisorption. f) Comparison of H_2 TPD for Ru-based catalysts where the value for mass spectrum $m/z = 2$ is normalized by the mass of catalyst.

limited by hydrogen inhibition at low temperatures. Indeed, the vast literature of conventional ruthenium catalysts typically lists the reaction order of hydrogen as negative (≈–1).[12–15]

In contrast to more conventional catalysts, the reaction order of H_2 with ruthenium supported on ceria is approximately zero, as shown in Figure 1b. The reasons behind the lack of hydrogen inhibition presented by the ceria support is believed to be related to the strong metal-support interaction between the Ru and the ceria promoting hydrogen spill-over from the active sites to the support as depicted in Figure 1c. This unique catalytic effect on hydrogen was confirmed through H_2 temperature programmed desorption (TPD) (Figure 1f). Ru/Cs/CNT and Ru/Al_2O_3 show two distinct desorption peaks roughly corresponding to bulk hydrogen adsorbed on the support (low-temperature peak) and hydrogen on Ru (high-temperature peak). One can notice that the light-off temperature (Figure 1e) coincides with the release of hydrogen from Ru. In comparison, $Ru/Cs/CeO_2$ only shows one large low-temperature desorption peak, with an overlap of the hydrogen desorption from the Ru surface and the support responsible for the low-temperature catalytic activity. Rather than simply involving hydrogen spill-over to surface hydroxyl groups on CeO_2[16]—which are also present on Al_2O_3—this process of hydrogen removal from Ru likely includes hydrogen incorporation into the ceria crystal, particularly through oxygen vacancies.[17] The high activity presented by Ru supported on nanostructured CeO_2 corroborate previous analyses of the structural sensitivity of Ru/CeO_2,[18] and the use of lanthanide series oxides as promoters to effectively remove hydrogen inhibition.[19,20] In addition, nanostructured ceria rods (NR) have previously shown enhanced catalytic activities in oxidation reactions due to enhanced electronic promotion of oxygen vacancies.[21,22] It is important to mention that although incipient wetness impregnation of ruthenium nitrosyl nitrate leads to larger (5–10 nm) Ru NPs than the theoretical optimum, they show good anchoring in the support with a strong metal-support interaction (Figure 1a and Figure S2, Supporting Information). Indeed, good stability of the $5\%Ru/10\%Cs/CeO_2$ catalyst was confirmed by a constant particle size (10 nm) before and after reaction as determined by CO chemisorption.

Ammonia synthesis occurs through a sequence of elementary reactions, being the dissociative adsorption of nitrogen the limiting step at low temperatures.[14,15] A reaction order of approximately unity for nitrogen is indicative of this reaction mechanism and was confirmed for the $5\%Ru/10\%Cs/CeO_2$ catalyst (Figure 1b). Electronic promotion of ruthenium is well known to increase ruthenium activity both through increasing the rate of nitrogen dissociation[23] and through promoting the desorption of ammonia (and other NH_x species) on the ruthenium surface through repulsion between electrons and a Lewis acid. Removing ammonia from the surface decreases the reaction order for NH_3 (≈0),[14,15,24] enhancing the kinetics which allows the catalyst to achieve high conversions near equilibrium, which is crucial for the combined catalyst-absorbent system. Cesium (Cs_2O under reaction conditions)[25] was chosen in this case for electronic promotion because of its low electronegativity and ability to donate electrons to ruthenium,[26] as depicted in Figure 1c. However, electronic promotion alone is not sufficient for an effective catalyst, as Ru/Cs/CNT is highly promoted through both Cs and conductive CNT,[27] but it still has a comparatively low activity (Figure 1e) due to H_2 inhibition.

These catalytic results present a breakthrough for the integration of the reaction and separation of ammonia to surpass the low equilibrium conversions at low temperature. While the vast majority of previously reported catalytic studies correctly target differential conditions not limited by equilibrium to evaluate their activity under kinetic control, herein, we aim for rapid near-equilibrium conversions and low temperatures. As such, the activity of $5\%Ru/10\%Cs/CeO_2$ was tested under a wide range of temperatures and conversions, as shown in Figure 1d, because the crucial characteristic of the catalyst is the entirety of the conversion profile—not just the low-conversion activity. For this reason, a direct comparison of reaction rate with other catalysts in the literature is not appropriate.

A kinetic model was developed for nanostructured ceria supported, cesium promoted ruthenium using a conventional rate law equation in terms of the reaction species partial pressure (bar) (Equation (1)). The robustness of the model with respect to both kinetics and equilibrium was improved by analyzing the catalyst under three different ratios of nitrogen to hydrogen (Figure 1d). As the N_2:H_2 ratio increases from the stoichiometric value (1:3 N_2:H_2), the rate increases in agreement with the experimental reaction orders (Figure 1b), and the equilibrium conversion decreases. As supported from literature, the reaction order for NH_3 in the forward reaction was assumed to be zero due to the electronic promotion provided by cesium.[24] The pre-exponential factor and activation energy of the forward reaction were determined using data under 5% conversion. These data follows an Arrhenius dependence even though it is >10% of the equilibrium conversion because the electronic promotion removes NH_3 from the surface.

Unlike most rate equations which only consider kinetics under differential conditions, the analysis of $5\%Ru/10\%Cs/CeO_2$ for in-situ separation required accurate inclusion of equilibrium into the rate law (i.e., the reverse reaction). The reverse rate constant was determined by defining the forward and reverse rates equal at equilibrium for a ratio of 1:3 N_2:H_2. The reaction order of NH_3 in the reverse reaction (1.3) was fit using the behavior of the catalyst at high NH_3 pressures (i.e., the curvature at high conversions), and the order of hydrogen in the reverse reaction was fit such that equilibrium is approximately followed for N_2:H_2 ratios of 1:1 and 2:1. The model closely describes the experimental data at different temperatures and N_2:H_2 ratios, as shown in Figure 1d, and is structurally similar to previous kinetics models for ammonia synthesis.[28]

$$\text{rate}\left(\frac{\text{mol}}{g_{\text{cat}}\ \text{min}}\right) = k_1\ P_{N_2} - k_{-1}P_{NH_3}^{1.3}P_{H_2}^{-2.5}\ \text{where}$$
$$k_1\left(\frac{\text{mol}}{g_{\text{cat}}\ \text{min bar}}\right) = 2.9\cdot e^{-62139/RT(K)} \quad (1)$$
$$k_{-1}\left(\frac{\text{mol}}{g_{\text{cat}}\ \text{min bar}^{-1.2}}\right) = 2.31\cdot 10^{9}\cdot e^{-133714/RT(K)}$$

2.2. Absorbent Development and Kinetic Model

The integrated ammonia synthesis and absorption requires the design of a resistant absorbent capable of retaining ammonia at relatively high temperatures aligned with its synthesis. We have achieved this by supporting manganese chloride in silica

($MnCl_2/SiO_2$). $MnCl_2$ desorbs water and ammonia at different temperatures, avoiding the formation of acid and thus its consequent decomposition. This is a unique property in comparison to magnesium chloride ($MgCl_2$) and calcium chloride ($CaCl_2$), conventional absorbents for ammonia separation due to their plentifulness.[5,29–31] $CaCl_2$ does not absorb ammonia at reasonable ammonia partial pressures above 300 °C and therefore is not suitable for a combined catalyst-absorbent process.[32] While $MgCl_2$ is known to retain ammonia up to almost 400 °C, its implementation is severely hindered by its decomposition which releases hydrogen chloride. $MgCl_2$ absorbs water from the air (like other absorbents) and shows a strong preference to decompose to magnesium oxide and hydrogen chloride when heated above 300 °C rather than releasing water. Even when put under <10 µbar vacuum and 200 °C for several hours, chemical bounded water ($MgCl_2 \cdot H_2O$) remains. When heated > 300 °C under N_2, it slowly decomposes forming acid as evidenced by pH paper over the vessel outlet. We demonstrate that even negligible amounts of water are capable of degrading the catalyst in contact with the absorbent at high temperatures (Figure S8b, Supporting Information), preventing the successful integration of both materials. The decomposition of $MgCl_2 \cdot H_2O$ is a problem that has plagued chemists in the electronics industry for some time[33,34] and the steps involved in the mechanism are well established.[35,36] Indeed, decomposition is likely the cause of inconsistent and contradictory results in previous attempts at a combined catalyst-absorbent system.[37]

Unlike $MgCl_2$, manganese chloride ($MnCl_2$) releases water at considerable lower temperatures (<200 °C), making it stable at high temperatures,[38] while also retaining ammonia to similar temperatures as $MgCl_2$.[6] This resistance to decomposition was confirmed by heating fully hydrated $MnCl_2 \cdot H_2O$ to 190 °C under N_2 and measuring the change in mass, which indicated complete release of water down to ≈1%. No decomposition was apparent either from pH paper over the effluent of the vessel or in a color change from pink ($MnCl_2 \cdot H_2O$) to green (MnO). The study of $MnCl_2$ was included in the development of many absorbents over the recent decades for thermal energy storage,[39,40] however it has heretofore been ignored in ammonia separation[5] because the importance of its unique characteristics in relation to water and ammonia has not been recognized.

As with other absorbents,[29] pure $MnCl_2$ is unstable, decreasing its absorption capacity over the first ≈4 absorption–desorption cycles, as shown in **Figure 2**b, before reaching a steady-state operation. Absorption is known to involve the incorporation of ammonia into the lattice of the salt (Figure 2a, 2nd and 3rd Steps), causing an expansion of the crystal structure which leads to agglomeration and a consequent decrease in surface area, as shown by the surface area of fresh and used (i.e., cycled) $MnCl_2$ in **Table 1**. To minimize this effect, $MnCl_2$ was dispersed on several supports including Al_2O_3, carbon nanotubes (CNT) and SiO_2. In all cases, the absorbent effectiveness increases respect to the unsupported $MnCl_2$ as shown in Figure 2c. 50% $MnCl_2/SiO_2$ shows a higher ammonia absorption than 50% $MnCl_2/Al_2O_3$ due to the larger surface area of the former (Table 1). This surface area only partially decreases between the fresh and used absorbent due to the blocking of smaller pores of the support by the absorbent (Table 1), but it does not alter the absorbent effectiveness (Figure S5, Supporting Information). CNT have a surface area similar to SiO_2 but have lower surface area after loading $MnCl_2$ due to the higher weight percent $MnCl_2$ and the clogging of the microporous structure of CNT, leading to diminished absorbent performance (Figure 2c).

Absorption involves a chemical reaction (rather than a physical interaction) and therefore its kinetics can be described with an equilibrium constant which follows the van't Hoff relation. The equilibrium constant simplifies to an equilibrium pressure of ammonia after removing solid species. Above the equilibrium pressure, absorption occurs to completion assuming excess ammonia. Absorption occurs in multiple steps that usually approximate to molar equivalents of the absorbent salt (e.g., 1,2,4 for $MgCl_2$), but $MnCl_2$ has the unique property that the first absorption stage is divided into approximately 0.5 and 1 molar equivalents, as shown is Figure 2a and Equations (2) and (3). This property is evidenced by the current analysis to model $MnCl_2/SiO_2$ in agreement with previous results.[6]

$$MnCl_2 + 0.5NH_3 \leftrightarrow MnCl_2 \cdot 0.5NH_3 \quad K_1 = 1/P_{eq1}^{0.5} \tag{2}$$

$$MnCl_2 \cdot 0.5NH_3 + 0.5NH_3 \leftrightarrow MnCl_2 \cdot NH_3 \quad K_2 = 1/P_{eq2}^{0.5} \tag{3}$$

The experimental data of ammonia separation on 50 wt% $MnCl_2/SiO_2$ shows an unexpected phenomena with almost complete removal of ammonia (>95%) between 0 and 30 min even though the equilibrium pressures for 0.5 and 1 molar equivalents of ammonia is above the partial pressure in the system (≈0.05 bar). This reproducible phenomenon is not apparent for either pure $MnCl_2$ or silica gel, but is present in a lesser degree for $MnCl_2/Al_2O_3$ (Figure S5, Supporting Information), and therefore it likely results from an interaction between $MnCl_2$ and the support. As illustrated in Figure 2a (1st Step), ammonia is believed to interact with the supported $MnCl_2$ by physical adsorption. Thus, the kinetics of ammonia separation in $MnCl_2/SiO_2$ (Figure 2d) is modeled with a three step process (Equation (4)) that uses a difference in ammonia pressure as the driving force and includes a general term for the fraction of capacity reached (X_A^k) in each step (k) due to ammonia accumulation in the absorbent. This overall process is hereafter referred to as "sorption" to distinguish it from adsorption (1st term) and absorption (2nd and 3rd terms). This three step sorption process is confirmed by incrementally increasing the ammonia pressure and comparing the ammonia experimentally removed to the prediction of the model, as shown in Figure 2e. While holding the temperature constant (350 °C), the pressure of ammonia was increased incrementally from 0.25 to 0.85 to 1.75 bar NH_3 to specifically target each step in the model. The initial rate of ammonia removal for each case shows a close similarity with the model however, over-time the model begins to diverge from the experimental data because the highly inhomogeneous structure of the thickly loaded salt makes precise or analytical description of the dynamic sorption process infeasible.

$$\text{rate}\left(\frac{\text{mol}}{g_{MnCl_2}\,\text{min}}\right) = 3\cdot10^{-4}\left(P_{NH_3} - 0.05\right)\left(1 - X_A^1\right) + 2\cdot10^{-2}\left(P_{NH_3} - P_{eq1}\right)^4\left(1 - X_A^2\right)^4 + 2.5\cdot10^{-2}\left(P_{NH_3} - P_{eq2}\right)^4\left(1 - X_A^3\right)^6 \tag{4}$$

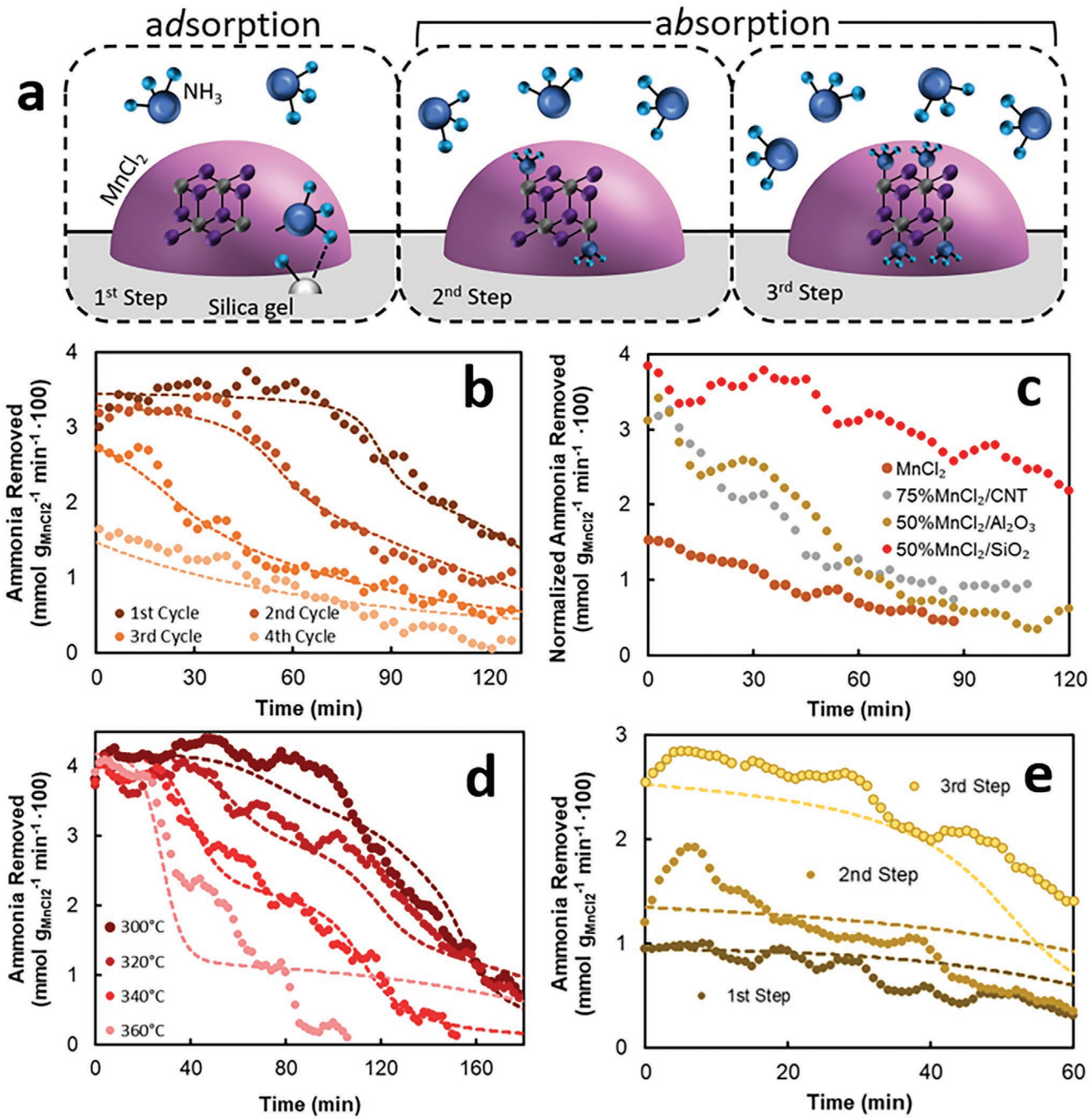

Figure 2. Ammonia absorption. a) Schematic of the three step of ammonia separation in which the system proceeds from adsorption, at low ammonia pressure, to absorption of 0.5 and 1 molar equivalents of NH_3, each requiring higher pressures of NH_3. b) Ammonia removed as a function of time with pure $MnCl_2$ at 320 °C and ≈1 bar NH_3 partial pressure. Dashed lines indicate the fitting of the data (Equation (4)) as surface area decreases. c) Comparison of the absorption performance of $MnCl_2$ and supported counterparts. Y-axis is normalized with repect to pressure of ammonia for each test to account for experimental fluctuations. d) Ammonia removed by 50 wt% $MnCl_2/SiO_2$ over time as a function of temperature with ≈1 bar NH_3. Dashed lines indicate the data fits with the model (Equation (4)). e) Ammonia removed over time when isolating each step by incrementalling increasing NH_3 pressure from 0.25 to 0.85 bar to 1.75 bar with 50 wt% $MnCl_2/SiO_2$ at 350 °C. Dashed lines indicate the prediction of each term in the model (Equation (4)).

A high order (4th order) driving force for absorption fit the trend in Figure 2d that rate drops quickly with temperature even before equilibrium is reached, and is in agreement with previous results suggesting exponential dependence.[32] The high order dependence on accumulation attempts to lump together the effect of ammonia diffusing through growing shells of reacted $MnCl_2 \cdot 0.5NH_3/MnCl_2 \cdot NH_3$ in individual particles and the variability of particle morphology. Similar to

Table 1. Surface area and pore size of supported absorbents and supports.

Material	BET surface area [$m^2 g^{-1}$]	BJH average pore size [nm]
Fresh $MnCl_2$	13	NA
Used $MnCl_2$	0.8[a)]	NA
Silica gel (SiO_2)	330	9
Fresh 50 wt% $MnCl_2/SiO_2$	128	9
Used 50 wt, %$MnCl_2/SiO_2$	92	17
Y-Alumina (Al_2O_3)	74	17
Used 50 wt% $MnCl_2/Al_2O_3$	29	30
Carbon nanotubes (CNT)	195	≈2 nm[b)]
Used 75 wt% $MnCl_2$/CNT	44	≈2 nm[b)]

[a)]This value is below the detection level of the equipment, and therefore highly uncertain; [b)]The pore size was determined from the pore size distribution rather than the BJH average.

Figure 2e, the change in rate of sorption over long times in Figure 2d shows the most deviation between model and data due to the difficulty in describing the dynamic absorption process. The model for 50 wt% $MnCl_2/SiO_2$ was also used to describe pure $MnCl_2$ (Figure 2b) by removing the first term (adsorption) and re-fitting the kinetic constants. When applied to the first four cycles of absorption for pure $MnCl_2$, the model indicates a decrease in surface area of several orders of magnitude (Figure S4, Supporting Information), thus confirming the surface area measurements (Table 1) and suggesting the surface area of used $MnCl_2$ may in fact be much lower than measurable.

2.3. Integration of Ammonia Synthesis and Separation—Combined Catalyst-Absorbent System

The integration of the ammonia synthesis and separation by combining the catalyst and absorbent beds demonstrates, for the first time, the achievement of conversions above equilibrium in a single pass. For this, segregated catalyst-absorbent layers in series were used as depicted in **Figure 3**a (see Experimental Section for further details). A high conversion near equilibrium is achieved in the first bed before switching flow to the rest of the beds in series. The change in total gas flow is recorded as a function of time (Figure 3b). As both ammonia synthesis and ammonia sorption cause the flow through the system to decrease, the previously developed catalyst and absorbent kinetic models were used to estimate the conversion achieved. The model uses the experimentally measured conversion of the first catalyst bed as an input, and applies the absorbent and catalyst models to subsequent beds to numerically calculate the predicted change in gas flow and the corresponding conversion. To partially remove the effect of dispersion on the results (i.e., a non-instantaneous change in flow after switching valves), time zero is defined as the point when the change in flow exceeds that predicted by sorption alone. Temperature, N_2:H_2 ratio, and number of catalyst-absorbent layers were varied to assess the ability of the model to predict the performance of the combined catalyst-absorbent system.

As shown in Figure 3b, there is generally a good agreement between the experimentally measured change in flow and the prediction of the conversion model (additional results are shown in Figure S7, Supporting Information). The spike in conversion at short times is an artifact created by the back pressure regulator which reacts sharply to keep the system pressure constant after the sudden drop in flow when switching from the first catalytic bed to the all beds in series. At longer times, the small differences between the model and experimental measurements is believed to be caused by the incomplete understanding of how the rate of sorption changes with time as a result of inhomogeneity in the structure of the absorbent, as previous discussed. Additionally, in the case of a double-layer system, it is apparent that the model could be over predicting the achieved conversion. It is likely that this discrepancy is due to the third catalyst bed being partially degraded (Figure S8c, Supporting Information). During the catalyst reduction process, the second catalyst bed might release water (or another chemical) that interacts with the absorbent, causing it to slightly decompose and consequently degrade the third catalyst bed. These observations highlight the importance of careful design of the integrated system with a special focus on material compatibility prior (i.e., activation) and during the operation of the system.

The approximate conversion achieved during the first 30 min as estimated using the model when coupling catalyst and absorbent beds in series is shown in Figure 3c. The conversion exceeds equilibrium in all cases to varying degrees depending on the experimental conditions. A ratio of 1:1 N_2:H_2 leads to the highest conversion because it effectively balances the conversion achieved by the catalyst with the increase in sorption rate at lower temperatures. A ratio of 2:1 N_2:H_2 is similarly able to exceed equilibrium by a wide margin, but the conversion is lower due to the greater limitation of the reaction equilibrium compared to the other cases. For all three N_2:H_2 ratios, the increase in conversion is almost doubled when moving from a single-layer to a double-layer configuration as expected, providing essential guidance for the design of the active bed system for the deployment of this new Haber-Bosch-based technology.

2.4. Design of Integrated Catalyst–Absorption Systems

By using the developed models for catalyst and absorbent performance capable of successfully predicting the effect of the integrated synthesis and separation, the parameters and constrains for a system designed to effectively synthesize ammonia in a single vessel are explored. An ideal plug flow system was chosen as the basic design configuration to mirror the smaller scale experimental system presented above. The primary design constraint is the conversion of hydrogen due to its energy intensive production. Thus, it was set to be above 95% when the integrated system begins operation and the system is considered no longer operational when it drops below 90%. It is important to highlight that this is a dynamic system as the absorbent fills up during operation. Only N_2:H_2 ratios above the stoichiometric value of 1:3 are considered, due to the low energy cost of N_2 production relative to H_2. As a starting point, the size of the absorbent sections is set to achieve a residence

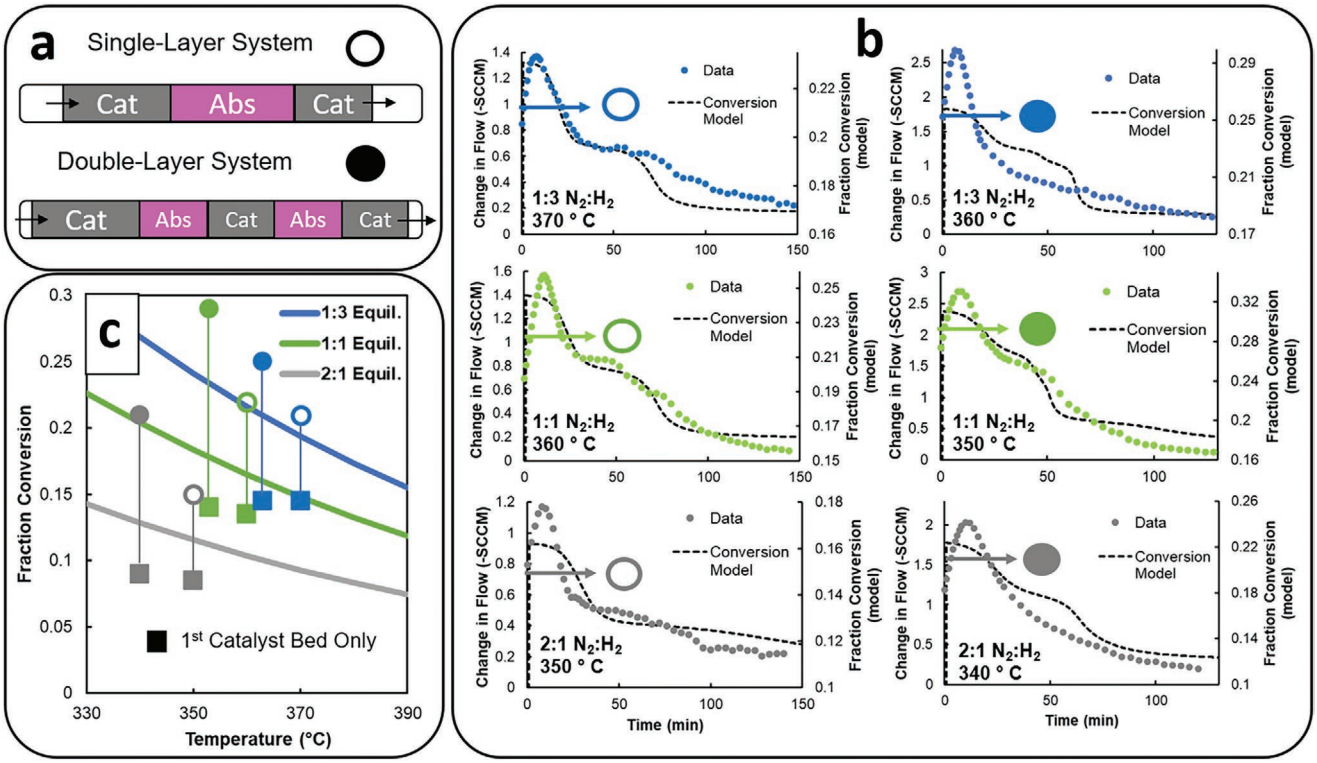

Figure 3. Integrated catalyst-absorbent system. a) Schematic of the configurations for two catalyst-absorbent systems. The first catalyst layer is both systems was 300 mg 5%Ru/10%Cs/CeO_2. The additional catalyst beds contained 200 and 150 mg, and the absorbent beds were 900 and 750 mg of 50 wt% $MnCl_2/SiO_2$ in the single-layer and double-layer systems, respectively. b) Comparison of measured change in flow to that predicted by the model and the corresponding estimated fractional conversion by the model. The negative change in flow due to ammonia synthesis/absorption is shown on a positive axis to facilitate the visualization. The approximate maximum change in flow and conversion is represented by arrows and further depicted by open/filled circles in (c). c) Summary of the approximate conversion during the first 30 min compared to equilibrium (solid lines) for 1:3, 1:1, and 2:1 ratio of N_2:H_2.

time of 0.1 min for a given inlet flow rate. The number of layers (catalyst + absorbent) is then adjusted to achieve > 95% hydrogen conversion at the start of operation at a given temperature, pressure, N_2:H_2 ratio, and catalyst:absorbent volume ratio. With each layer, the total amount of flow decreases and the conversion increases along the length of the reactor, as depicted in **Figure 4**a.

A sensitivity analysis of the effect of temperature, N_2:H_2 ratio, and catalyst:absorbent volume ratio on the total amount of ammonia produced by the system during operation (mmol cm^{-3}) and the productivity of the system over the time of operation (mmol cm^{-3} min^{-1}) was carried out at a system pressure of 20 barg. For every N_2:H_2 ratio, the overall optimum of productivity occurs at a catalyst:absorbent volume ratio ≈1 (all data in Table S9, Supporting Information) so this value was fixed for comparison. As shown in Figure 4b, for each N_2:H_2 ratio, there occurs a minimum in the number of layers required as a function of temperature. At higher temperatures, the number of layers increases due to the equilibrium limitation (i.e., amount of ammonia each catalyst layer can produce), while at lower temperatures the number of layers increases due to the diminished kinetic activity of the catalyst.

As opposed to the size (i.e., number of layers) of the vessel (i.e., integrated reactor), which is determined by the properties of the catalyst, the production of ammonia and system productivity are determined by the absorbent. As shown in Figure 4c, the total ammonia production increases as the temperature decreases because the absorbent is able to retain effectiveness for a longer period of time. It is important to note that each of the points of Figure 4c corresponds to a different number of layers, as shown in the counterpart Figure 4b. Achieving >95% hydrogen conversion at the start of operation depends on the "adsorption" process, which removes nearly all of the ammonia for a short period of time and is not dependent on temperature within the range of the current model. In contrast, remaining >90% hydrogen conversion depends on the kinetics of absorption, which is strongly favored at lower temperatures. Therefore, at higher temperatures the system only operates for a short period of time within the design constrains—producing little ammonia—while at lower temperatures the system operates for a longer period of time—consequently producing much ammonia. This difference in the amount of time the system is able to operate also explains why the amount of ammonia produced per total vessel volume does not decrease at very low temperatures even as the number of layers approaches 100. With each additional layer, more absorbent is added to the system, allowing it to operate longer before reaching saturation and causing the total ammonia production to increase proportionally. However, once the amount of ammonia produced is normalized by the operational time of

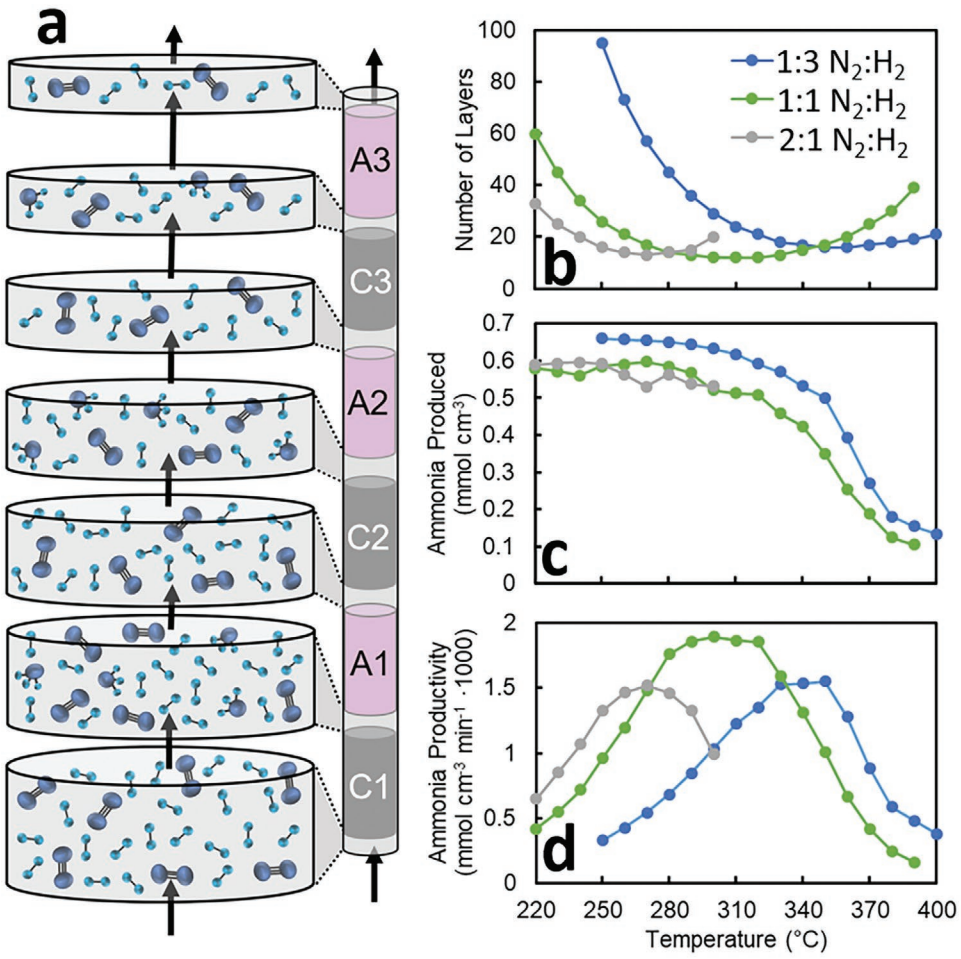

Figure 4. Design analysis of integrated flow system with 1:1 Catalyst:Absorbent volume ratio. a) Schematic depicting a decrease in flow after every layer of catalyst (CX) and absorbent (AX), where X represent the layer number. b) Number of layers required to reach > 95% H_2 conversion at the start of operating the flow system as a function of temperature and N_2:H_2 ratio. c) The amount of ammonia produced until H_2 conversion drops to < 90%, normalized by the total system volume. d) Ammonia productivity of the integrated system as defined by the amount of ammonia produced per volume per time.

the system (defined as system productivity, mmol cm^{-3} min^{-1}) there is a clear optimum for every N_2:H_2 ratio (Figure 4d) where the most ammonia is produced over the shortest time with the smallest vessel.

Additionally, while the results for system productivity in Figure 4d would strongly suggest that operating with a non-stoichiometric N_2:H_2 ratio is preferable, the model also indicates potential drawbacks. Unlike with a stoichiometric ratio—where N_2 and H_2 partial pressure remain approximately constant at the start of each layer—a higher N_2:H_2 ratio causes N_2 pressure to increase across the vessel due to excess N_2 flow. As a result, the partial pressure of ammonia produced in the catalyst layers near the end of the vessel is smaller than with a stoichiometric ratio. In some cases such as at >300 and >390 °C for N_2:H_2 2:1 and 1:1, respectively (Figure 4b–d), the resulting partial pressure of ammonia it is too low for ammonia to be removed by the absorbent and it is not possible to achieve >95% hydrogen conversion. This limitation is present even with the current $MnCl_2/SiO_2$ capable of removing ammonia to 0.05 bar partial pressure due to its initial *ad*sorption capability. Using a more conventional absorbent without this unique property will make the limitation of overall hydrogen conversion with a non-stoichiometric mixing more striking as simple absorption requires much higher ammonia partial pressure than 0.05 bar.

Decreasing the overall pressure of ammonia synthesis is often the focus of innovation because it would clearly decrease the energy and capital requirement to compress N_2 and H_2. Indeed, the pressure of the conventional recycle process has already been decreased from >100 to 20 bar by using an absorber because absorption can remove ammonia more completely than condensation.[4] However, further reductions of pressure are detrimental to the integrated system due to the ammonia partial pressure required for successful separation by absorption. The catalyst rate equation (Equation (1)) is linear with pressure, but when the system pressure is decreased from 20 to 10 to 5 barg the productivity of the integrated system drops from 1.5 to 0.4 to 0.1 mmol cm^{-3} min^{-1}·1000, respectively (Figure S10, Supporting Information). As the overall pressure decreases, the ammonia partial pressure attainable by the catalyst decreases and the kinetics of absorption are sharply

diminished until absorption is not possible. A system pressure of ≈20 bar is required for effective ammonia production because the higher reaction conversion drives absorption rather than simply due to kinetics improvements in the reaction.

The current model—while demonstrating important parameters for integrated system design—does not include the crucial aspect of regenerating the absorbent by decreasing pressure and/or increasing temperature to retrieve separated ammonia. This should be the focus of research considering the feasibility of the integrated system demonstrated herein. We envision a semi-batch flow system to periodically regenerate the absorbent once the overall conversion of hydrogen is <90%, similar to industrial absorption and adsorption systems. Its design will entail an additional optimization of the parameters relative to effectively retrieving ammonia. In particular, the ammonia needs to be desorbed from the absorbent and removed from the vessel without contacting the catalyst and decomposing back to N_2 and H_2.

3. Conclusions

Integrated ammonia synthesis and separation is herein demonstrated using a catalyst ($Ru/Cs/CeO_2$) that is not inhibited by hydrogen or ammonia and an absorbent ($MnCl_2/SiO_2$) that avoids decomposition by releasing water at much lower temperatures than ammonia. The temperature range for catalytic activity overlaps the range for ammonia absorption such that a flow system with catalyst and absorbent in series is able to achieve conversions beyond reaction equilibrium. Mathematical modeling of the long-term kinetics of the catalyst and absorbent facilitate the optimization of parameters associated with the design of an integrated system to maximize hydrogen conversion, revealing that size of the system (i.e., the number of catalyst + absorbent layers) depends primarily on the kinetics and equilibrium of the catalyst, while the ammonia produced over the time of operation depends on the effectiveness of the absorbent. Such a system is likely to operate at a N_2:H_2 ratio greater than stoichiometric to enhance catalyst kinetics at the expense of nitrogen underutilization. These results underpin the re-definition of the Haber-Bosch process where further technological development is required to regenerate the absorbent and retrieve the synthesized ammonia in an economical and efficient manner.

4. Experimental Section

Materials and Characterization: Ruthenium-based catalysts were synthesized by incipient wetness impregnation with ruthenium nitrosyl nitrate solutions of Y-alumina (99.97%, 3 micron powder, Alfa Aesar CAS: 1344-28-1), multi-walled carbon nanotubes (nanocyl NC7000) and nanostructured ceria rods, followed by drying at 80 °C under vacuum for ≈2 h. After depositing ruthenium, cesium was similarly deposited using a solution of cesium carbonate. Ceria nanorod support (Figure S2a, Supporting Information) was synthesized using the hydrothermal synthesis method described previously.[41] Briefly, cerium nitrate hexahydrate (1.2 g) was dissolved in 15 M NaOH and heated in an autoclave at 70 °C for 12 h before washing in water/ethanol and drying at 80 °C under vacuum. Catalysts were characterized by temperature program reduction (TPR) and H_2 temperature program desorption (TPD) using a Micromeritics Autochem II chemisorption analyzer equipped with a MKS Cirrus 2 mass spectrometer. Pulse CO chemisorption was conducted after reduction to 400 °C (reaction conditions) and the average particle size was calculated assuming a semi-spherical particle shape.[42] Microscopy pictures were taken using a FEI Tecnai F20 G2 200 kV FEGTEM microscope with a Gatan image filter (GIF) 200 followed by a 4 k × 4 k CCD detector. Specimens were prepared by sonicating a dispersion of catalyst in water followed by drop-casting onto carbon-coated Cu grids (Agar Scientific, 400 mesh).

Supported $MnCl_2$ absorbents were prepared by drying $MnCl_2{\cdot}4H_2O$ to $MnCl_2{\cdot}H_2O$ at 80 °C under vacuum slowly to prevent it from melting followed by multiple cycles of incipient wetness impregnation using ethanol with drying at 80 °C under vacuum for 2 h in-between each cycle. Absorbents were characterized by N_2 physisorption at 77 K using a Micromeritics ASAP 2020. The Brunauer–Emmett–Teller method was used to calculate surface area and average pore size was calculated from the Barrett–Joyner–Halenda method.

Experimental Procedure: All experiments were carried out in a bespoke rig shown in **Figure 5** equipped with mass flow controllers (MFCs, Bronkhorst EL-Flow Select) for N_2 and H_2 inlet flows, a reactor consisting of a 12 mm stainless steel tube with a 9.5 mm OD × 8 mm ID glass tube liner, an absorber of the same construction with a bed of absorbent (and additional layers of catalyst/absorbent in the case of the integrated system) and a back pressure regulator (BPR, Bronkhorst EL-Press) to keep the pressure in the system constant. The conversion was measured using a mass flow meter (MFM). The temperature in the reactor was controlled using a 12 in. cylindrical ceramic heater with insulation at the top and thermocouples outside the reactor and before the catalyst bed. The temperature in the absorber was controlled using a 0.5 in. high-temperature heating tape surrounded by fiberglass insulation with thermocouples before and after the absorbent bed. All equipment was interfaced with LabVIEW for continuous and rapid data collection.

In the typical catalytic experiment, a ≈2 cm catalytic bed was used consisting of 300 mg of the catalyst (200 mg in the case of 7% Ru loading) and course (40 grit) SiC to provide even spacing and gas flow. The catalyst was reduced in-situ using 10 mL min^{-1} H_2 at a ramp rate of 5 °C min^{-1} to 400 °C. The absorber for catalyst tests consisted of an excess of pure $MnCl_2$ (≈10 g) at ambient temperature to ensure that all ammonia from the reactor is removed. The reactions were carried out at 20 barg using a total flow of 11.7 mL min^{-1} of the desired N_2:H_2 ratio. After steady state was reached at 400 °C, the temperature was ramped down at a rate of 1 °C min^{-1}. Stability tests where temperature was ramped up and down several times showed consistent results. The catalytic activity remains stable over a week of runs (Figure S3, Supporting Information) however, the catalyst will lose activity if exposed to air, likely due to the migration of cesium from the surface of oxidized Ru NPs rather than the agglomeration of Ru NPs.[27] Ammonia conversion was calculated based on the change of flow using a flowmeter in the outlet stream with an experimental error of ±10%. Such error is associated to the rapidly (seconds) fluctuating signal changes in the flow when going from 20 to 1 bar through the BPR orifice. Such fluctuations are compensated by taking a moving average value. In addition, the BPR controls the pressure in the system with a response time of minutes which can slightly over/undershoot (≈10%) the desired pressure temporarily. This fluctuation is only partially removed by calculating a moving average. The ammonia conversion was confirmed by measuring the outlet stream composition using a gas chromatograph equipped with a thermo conductivity detector (TCD).

In a typical absorption experiment, a ≈4 cm absorbent bed was constructed. The mass of absorbent used varied from ≈1.1 g when testing 50% $MnCl_2/SiO_2$ or 50% $MnCl_2/Al_2O_3$ to 600 and 610 mg when testing 75% $MnCl_2$/CNT and pure $MnCl_2$, respectively, because the later absorbents also required course SiC (40grit) for spacing and had very low density in the case of 75% $MnCl_2$/CNT. Prior to the experiment, the absorbent was heated to 400 °C in 10 mL min^{-1} N_2/H_2 at 5 °C min^{-1} with a hold at 200 °C for 3 h to release all water. For the absorption experiments, ammonia was produced in situ using 5%Ru/10%Cs/CeO_2 as a catalyst at 20 barg, 330 °C and 11.7 mL min^{-1} 1:3 N_2:H_2 molar

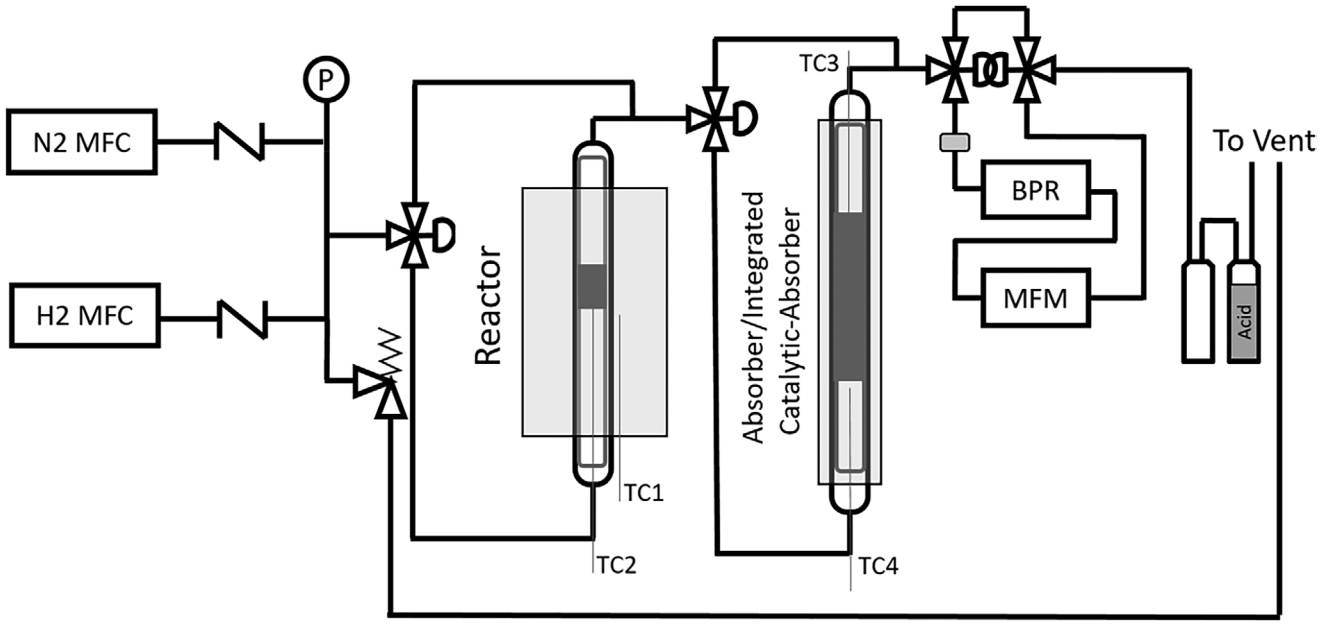

Figure 5. Schematic of experimental rig. The system conducts analysis through a change in flow between the MFCs and the MFM due to reaction and absorption. The back pressure regulator (BPR) keeps the system pressure constant. When analyzing a combined catalyst-absorbent system, the absorber contains both the absorbent bed and the 2nd/3rd catalyst beds in series.

flowrate. Absorption kinetics were measured once steady state was achieved. Once saturated, the absorber was regenerated by heating to 380 °C under N_2 for 1 h.

In a typical integrated catalyst-absorbent experiment, two reaction vessels were used at the same temperature. The reactor (Figure 5) was loaded with 300 mg of 5%Ru/10%Cs/CeO_2 as in the catalytic tests described above. The second vessel was loaded with both absorbent and second catalyst bed in the case of the single-layer configuration or two layers of absorbent and catalyst in the case of the double-layer configuration (Figure 3a). For the single layer configuration, 900 mg of 50% $MnCl_2/SiO_2$ was loaded in the absorber and dried at 425 °C before adding the second catalyst bed (200 mg 5%Ru/10%Cs/CeO_2). Air contact was minimized to avoid water absorption. For the double layer configuration (configuration shown in Figure 3a), the absorber was loaded with two beds of 750 mg each with the 2nd and 3rd catalyst beds of 150 mg 5%Ru/10%Cs/CeO_2 each. The analysis of the combined catalyst-absorbent system started with pressurizing the system (20 barg) with nitrogen only. Once the pressure was stabilized, the flow was switched to 11.7 mL min^{-1} of the desired N_2:H_2 ratio through the reactor while bypassing the second vessel. Once that the 1st catalyst bed had reached steady state, the flow was switched to pass through the second vessel. After each test, the absorbent was regenerated at 360 °C under 5 mL min^{-1} of N_2 for 2 h.

Modelling Framework: All models were constructed using numerical calculations in MATLAB where the catalyst and absorbent beds were discretized into differential segments where the concentration of all species is considered constant. The number of discretizations in each bed was a minimum of 100, but typically ≈1000 unless many beds were considered in series (i.e., combined catalyst-absorbent system). The time step of the numerical models was calculated as the time for the gas phase to pass through each discretization such that the effect of void volume in the reactor/absorber was also considered.

For the catalyst model, a conventional power law relation was implemented in which each kinetic parameter was determined using a distinct characteristic in the temperature-conversion profile obtained (Figure 1d). The order of reaction for N_2 and H_2 in the forward reaction was determined by varying the pressure of N_2 and H_2 independently and measuring rate of reaction (Figure 1f). These orders were confirmed by the increased catalytic activity as the N_2:H_2 ratio increased from 1:3 to 1:1 and 2:1. The rate constant for the forward reaction was calculated from an Arrhenius plot when conversion is <5%. Generating a model for the catalyst which included high conversion required discretization in 1000 segments because the reactor is no longer differential when the reverse reaction becomes significant. The reverse rate constant was determined assuming that the forward and reverse rates must be equal at equilibrium for 1:3 N_2:H_2. The order of reaction for NH_3 in the reverse reaction was determined by matching the discretized model with the curvature of the maximum conversion data. A higher order results in a model that reaches higher *peak* conversions because the reverse reaction requires a higher concentration of ammonia before it becomes significant relative to the forward reaction. Conversely, a lower order model achieves lower conversions because the reverse reaction needs to begin resisting the forward reaction at lower conversions if it will also maintain a hard-stop at equilibrium. Finally, the order of reaction for H_2 in the reverse reaction due to inhibition was determined using the constraint that the equilibrium is followed for N_2:H_2 ratios of 1:1 and 2:1 (i.e., a negative reaction order causes the conversion at high temperatures to decrease as N_2:H_2 increases because the reverse reaction becomes faster). This catalyst model is applicable at the wide range of temperatures, pressures, and N_2:H_2 ratios expected for a typical analysis.

The framework for the absorbent model of 50% $MnCl_2/SiO_2$—in which adsorption is added to two steps of absorption (Equation (4))—was motivated by i) its ability to initially remove nearly all ammonia regardless of temperature and ii) the variations in the decrease of absorption rate over time with different temperatures (Figure 2d). The latter is an indication of multiple absorption steps (0.5 and 1 molar equivalents) in agreement with previous results,[6] which were used to calculate the equilibrium constant of each step. For simplicity, the "adsorption" step was considered a quick consumption term independent of temperature. This assumption is acceptable despite the "adsorption" capacity being likely to increase at lower temperatures, as its magnitude is small relative to absorption at lower temperatures.

$$K_{eq1} = \frac{-42100}{8.314}\left(\frac{1}{T} - \frac{1}{650}\right) \quad (5)$$

$$K_{eq2} = \frac{-42100}{8.314}\left(\frac{1}{T} - \frac{1}{610}\right) \quad (6)$$

Few kinetic models have been developed with absorption/desorption for heat storage[43,44] and there is still much debate about how to best model the mechanism.[45] Nevertheless, the model developed herein incorporates the main terms for i). accumulation of ammonia and ii) the driving force (i.e., pressure relative to equilibrium) of each step, while approximating the temperature dependence of kinetic constants as being relatively insignificant over the range of temperatures studied. Eight parameters (capacity for each 3 steps, rate constant for each 3 steps, order for ammonia pressure relative to equilibrium in the absorption steps, and order for accumulation in the absorption steps) in this model were fit by methodically varying each one and measuring their effect on the change in the predicted ammonia removal by the model in a 1000 point discretized bed.

The capacity for "adsorption" was easily estimated as 13% of a molar equivalent of $MnCl_2$ based on the ammonia removed in the first ≈30 min. While the capacity for each step of absorption should theoretically be 0.5 molar equivalents each, a better fit of the experimental data was obtained at 0.35 molar equivalent. The difference between the theoretical and the experimental values is related to the partial $MnCl_2$ inaccessibility as a significant portion of the absorbent is likely to be either trapped in blocked pores of the silica gel or within a large $MnCl_2$ particle. The order for ammonia pressure relative to equilibrium in the absorption steps was fit as 4 because it generated a significant drop in rate at higher temperatures (i.e., higher equilibrium pressure) that was apparent in the data even though equilibrium had not been reached. A higher order dependence on ammonia pressure relative to equilibrium was also reported previously.[32] The high order (4 and 6) with respect to accumulation in the absorption steps was a result of large inhomogeneities in particle size and morphology, which causes different particles to reach absorption saturation or experience a significant drop in rate at different times. When representing the ammonia removed over time by the model (Figure 2d), the high order was reflected in the sharpness of the decrease in rate as the absorbent fills over time (i.e., the higher order, the sharper drop). It is important to note that this model is likely not applicable at high temperatures (>400 °C) because the absorbent might degrade or very high ammonia pressures because the mechanism may change.

These two catalyst and absorption models set the foundation for the prediction of the conversion using an integrated catalyst and absorbent system. Such integrated conversion model was validated using the experimental results for a single-layer or double-layer system (Figure 3a) using 500 discretizations for each catalyst and absorbent bed. For the simulation of integrated synthesis-separation flow systems, the number of layers (catalyst+absorbent) to initially reach 95% H_2 conversion was determined by repeatedly simulating a single layer (200 discretizations) where its input concentration $N_2/H_2/NH_3$ was determined by the previous layer. A maximum number of 100 layers was imposed. The number of layers was then used to simulate the entire vessel (all layers, 200 discretizations each) simultaneously over time to determine the amount of ammonia produced until H_2 conversion dropped to <90%. The residence time of the absorbent bed was arbitrarily set at 0.1 min and the residence time of the catalyst bed was scaled accordingly. The ratio of catalyst to absorbent was conducted in terms of volume. Nevertheless, the densities of catalyst and absorbent ($MnCl_2$) were approximated to be 0.24 and 0.25 g cm^{-3} and thus, the volume ratio was very similar to mass ratio. The flow of N_2/H_2 into the vessel was arbitrarily set at 0.1 mL min^{-1} however, it is important to note that the values of produced ammonia were normalized by the volume of catalyst and absorbent.

Supporting Information

Supporting Information is available from the Wiley Online Library or from the author.

Acknowledgements

L.T.M. would like to acknowledge the UK Engineering and Physical Science Research Council for her Fellowship award (grant number EP/L020432/2) and grant EP/N013778/1. CS is thankful to The Cambridge Trust for partially funding his scholarship.

Conflict of Interest

The authors declare no conflict of interest.

Data availability statement

The data that support the findings of this study are available in Cambridge research repository Apollo at [https://doi.org/10.17863/CAM.64285].

Keywords

absorption, ammonia synthesis, green ammonia, Haber-Bosch

Received: December 11, 2020
Revised: January 18, 2021
Published online: February 28, 2021

[1] J. W. Erisman, M. A. Sutton, J. Galloway, Z. Klimont, W. Winiwarter, *Nat. Geosci.* **2008**, *1*, 636.
[2] C. Smith, A. K. Hill, L. Torrente-Murciano, *Energy Environ. Sci.* **2020**, *13*, 331.
[3] W. H. Avery, *Int. J. Hydrogen Energy* **1988**, *13*, 761.
[4] M. Malmali, Y. M. Wei, A. McCormick, E. L. Cussler, *Ind. Eng. Chem. Res.* **2016**, *55*, 8922.
[5] M. Malmali, G. Le, J. Hendrickson, J. Prince, A. V. McCormick, E. L. Cussler, *ACS Sustainable Chem. Eng.* **2018**, *6*, 6536.
[6] R. Z. Sorensen, J. S. Hummelshoj, A. Klerke, J. B. Reves, T. Vegge, J. K. Norskov, C. H. Christensen, *J. Am. Chem. Soc.* **2008**, *130*, 8660.
[7] C. Smith, A. V. Mccormick, E. L. Cussler, *ACS Sustainable Chem. Eng.* **2019**, *7*, 4019.
[8] Z. Kowalczyk, S. Jodzis, J. Sentek, *Appl. Catal., A* **1996**, *138*, 83.
[9] S. Dahl, A. Logadottir, R. C. Egeberg, J. H. Larsen, I. Chorkendorff, E. Törnqvist, J. K. NØrskov, *Phys. Rev. Lett.* **1999**, *83*, 1814.
[10] S. Dahl, E. Tornqvist, I. Chorkendorff, *J. Catal.* **2000**, *192*, 381.
[11] C. J. H. Jacobsen, S. Dahl, P. L. Hansen, E. Tornqvist, L. Jensen, H. Topsoe, D. V. Prip, P. B. Moenshaug, I. Chorkendorff, *J. Mol. Catal. A: Chem.* **2000**, *163*, 19.
[12] S. Dahl, A. Logadottir, C. J. H. Jacobsen, J. K. Norskov, *Appl. Catal. A* **2001**, *222*, 19.
[13] K. Urabe, K. I. Aika, A. Ozaki, *J. Catal.* **1976**, *42*, 197.
[14] F. Rosowski, A. Hornung, O. Hinrichsen, D. Herein, M. Muhler, G. Ertl, *Appl. Catal., A* **1997**, *151*, 443.
[15] K. i. Aika, *Catal. Today* **2017**, *286*, 14.
[16] D. R. Mullins, *Surf. Sci. Rep.* **2015**, *70*, 42.
[17] N. Sakai, K. Yamaji, T. Horita, H. Yokokawa, Y. Hirata, S. Sameshima, Y. Nigara, J. Mizusaki, *Solid State Ionics* **1999**, *125*, 325.
[18] Z. Ma, S. Zhao, X. Pei, X. Xiong, B. Hu, *Catal.: Sci. Technol.* **2017**, *7*, 191.
[19] Y. Kadowaki, K. I. Aika, *J. Catal.* **1996**, *161*, 178.
[20] Z. Wang, B. Liu, J. Lin, *Appl. Catal., A* **2013**, *458*, 130.
[21] B. Y. Lin, Y. Liu, L. Heng, X. Y. Wang, J. Ni, J. X. Lin, L. L. Jiang, *Ind. Eng. Chem. Res.* **2018**, *57*, 9127.
[22] J. M. Lopez, A. L. Gilbank, T. Garcia, B. Solsona, S. Agouram, L. Torrente-Murciano, *Appl. Catal., B* **2015**, *174*, 403.
[23] J. Kubota, K. Aika, *J. Phys. Chem.* **1994**, *98*, 11293.

[24] K. Aika, M. Kumasaka, T. Oma, O. Kato, H. Matsuda, N. Watanabe, K. Yamazaki, A. Ozaki, T. Onishi, *Appl. Catal.* **1986**, *28*, 57.
[25] A. K. Hill, L. Torrente-Murciano, *Int. J. Hydrogen Energy* **2014**, *39*, 7646.
[26] K. I. Aika, T. Kawahara, S. Murata, T. Onishi, *Bull. Chem. Soc. Jpn.* **1990**, *63*, 1221.
[27] A. K. Hill, L. Torrente-Murciano, *Appl. Catal. B* **2015**, *172*, 129.
[28] D. Annable, *Chem. Eng. Sci.* **1952**, *1*, 145.
[29] K. Wagner, M. Malmali, C. Smith, A. McCormick, E. L. Cussler, M. Zhu, N. C. A. Seaton, *AIChE J.* **2017**, *63*, 3058.
[30] C. Y. Liu, K. I. Aika, *Ind. Eng. Chem. Res.* **2004**, *43*, 7484.
[31] M. J. Palys, A. McCormick, E. L. Cussler, P. Daoutidis, *Processes* **2018**, *6*, 91.
[32] C. Smith, M. Malmali, C. Y. Liu, A. V. McCormick, E. L. Cussler, *ACS Sustainable Chem. Eng.* **2018**, *6*, 11827.
[33] H. C. Eom, H. Park, H. S. Yoon, *Adv. Powder Technol.* **2010**, *21*, 125.
[34] O. G. Sivilotti, J. V. Sang, R. J. R. Lemay, *US Patent US005514359A*, **1994**.
[35] Q. Z. Huang, G. M. Lu, J. Wang, J. G. Yu, *J. Anal. Appl. Pyrolysis* **2011**, *91*, 159.
[36] Y. Kirsh, S. Yariv, S. Shoval, *J. Therm. Anal.* **1987**, *32*, 393.
[37] D. K. Ojha, M. J. Kale, A. V. McCormick, M. Reese, M. Malmali, P. Dauenhauer, E. L. Cussler, *ACS Sustainable Chem. Eng.* **2019**, *7*, 18785.
[38] O. G. Polyachenok, E. N. Dudkina, L. D. Polyachenok, *J. Chem. Thermodyn.* **2009**, *41*, 414.
[39] M. Mbaye, Z. Aidoun, V. Valkov, A. Legault, *Appl. Therm. Eng.* **1998**, *18*, 131.
[40] T. X. Li, R. Z. Wang, J. K. Kiplagat, L. W. Wang, *Appl. Energy* **2009**, *86*, 1201.
[41] L. Torrente-Murciano, A. Gilbank, B. Puertolas, T. Garcia, B. Solsona, D. Chadwick, *Appl. Catal., B* **2013**, *132*, 116.
[42] L. Torrente-Murciano, *J. Nanopart. Res.* **2016**, *18*, 87.
[43] M. Lebrun, B. Spinner, *Chem. Eng. Sci.* **1990**, *45*, 1743.
[44] V. Goetz, A. Marty, *Chem. Eng. Sci.* **1992**, *47*, 4445.
[45] G. L. An, L. W. Wang, J. Gao, R. Z. Wang, *Renewable Sustainable Energy Rev.* **2018**, *91*, 783.